Research Square

Preprints are preliminary reports that have not undergone peer review.
They should not be considered conclusive, used to inform clinical practice,
or referenced by the media as validated information.

Conflicting-aromatic Ba3B8: a fluxional binary nanocluster rotor †

Shuting Zhang
Xinzhou Normal University
Lizhao Fan
Xinzhou Normal University
Xiaobo Hu
Xinzhou Normal University
Yuzhen Du
Xinzhou Normal University
Tinglu Zhang
Xinzhou Normal University
Yingchao Ma
Xinzhou Normal University
Jinglu Guo
Xinzhou Normal University
Jingying Li
Xinzhou Normal University
Changqing Miao
Xinzhou Normal University
Yingjin Wang
Xinzhou Normal University
Linyan Feng
xzfenglinyan@126.com
Xinzhou Normal University

Research Article

Keywords: Boron-based alloy clusters, Dynamic structural fluxionality, Chemical bonding, Conflicting aromaticity, Molecular rotor

Posted Date: October 27th, 2026

DOI: https://doi.org/10.21203/rs.3.rs-11302720/v1

License: This work is licensed under a Creative Commons Attribution 4.0 International License.
Read Full License

Additional Declarations: No competing interests reported.

Abstract

Boron-based alloy clusters represent a fertile ground for exploring exotic chemical bonding and inherent structural fluxionality. Herein, we theoretically investigate the dynamic fluxionality and bonding characteristics of the three-layered Ba_3B_8 cluster *via* quantum chemical calculations, which adopts an inverted sandwich geometry. The distorted B_8 wheel is sandwiched between an upper Ba_2 dimer and an isolated Ba atom at the bottom. Born–Oppenheimer molecular dynamics simulation demonstrates that the Ba_2 dimer rotates unconstrainedly and glides atop the B_8 wheel at room temperature (298K). The rotation barrier is only 0.04 kcal mol^{-1} at the single-point CCSD(T) level. Chemical bonding analyses reveal that this system can be formulated as $[Ba_2]^{2+}[B_8]^{4-}[Ba]^{2+}$ ionic complex, where the $[B_8]^{4-}$ motif exhibits conflicting aromaticity with 8π/6σ electron delocalized. Strong interlayer electrostatic interactions (exceeding 15.8 eV) and fully delocalized π/σ electrons in the B_8 wheel synergistically enable the unhindered rotation of the Ba_2
dimer. The present Ba_3B_8 cluster expands the library of subnanoscale molecular rotors and provides a novel prototype for fluxional clusters featuring conflicting aromaticity.

1. Introduction

As a neighbor of carbon in the periodic table, boron chemistry remains far less developed than that of carbon. Owing to boron's inherent electron deficiency, boron clusters adopt distinctive geometric structures and exhibit unconventional multicenter bonding characteristics. Since the 1980s, researchers have systematically investigated the structural, electronic, and chemical bonding properties of pure boron clusters through combined photoelectron spectroscopy (PES) experiments and theoretical calculations [–]. These studies established that planar or quasi-planar structures prevail in boron clusters over a wide size range, and their thermodynamic stability is governed by delocalized multicenter π/σ bonds [6,15]. Accordingly, the chemical bonding concepts such as double aromaticity, antiaromaticity, multifold aromaticity, and conflicting aromaticity have been proposed to interpret their thermodynamic stability. Meanwhile, the electron-delocalized nature of boron skeletons also endows boron-based nanoclusters with prominent dynamic structural fluxionality [16–18].

Boron-based molecular rotors represent a hot topic in the field of nanomachines. In 2010, Huang and co-workers spectroscopically identified the B_{19}^- cluster, which Merino *et al.* further identified as a Wankel motor [10,]. Subsequently, quasi-planar bare boron clusters of B_{13}^+ and B_{18}^{2-} were also confirmed to exhibit dynamic fluxionality properties, wherein their peripheral boron ring rotate freely around the inner core [,]. Intriguingly, the dynamic fluxionality of B_{13}^+ was unambiguously validated *via* infrared experiments in 2017 []. Subnanoscale tank treads were reported for elongated boron-based clusters in the Zhai group, such as $B_{11}^{0/-}$ and B_{15}^+ [,]. Almost all of these boron rotors exhibit the delocalized π/σ bonds and possess multifold aromatic character.

Metal doping has proven to be an effective strategy for discovering novel boron-based nanorotors and expanding the library of boron-based nanoclusters [–]. Two-layered fluxional metal–boron frameworks including Mg_2B_8, M_2B_8 (M = Zn, Cd, Hg), Mg_2BeB_8, and $MB_7Zn_2^-$ (M = Be, Ru, Os) were reported in recent literature [–], which exhibit dynamic fluxional behavior at the interlayer between metallic units and boron motifs. Many three-layer sandwich structures with dual dynamic fluxional behavior have been reported, such as $Be_6B_{11}^-$, $Be_6B_{10}^{2-}$, $Na_6B_7^-$, $Na_8B_7^+$, and $Rb_6Be_2B_6$ clusters [–]. In particular, the $Be_6B_{11}^-$ sandwich exhibits the free rotational motion of the peripheral B_{11} ring and the central Be_6 prism, as well as the relative rotation between the two Be_3 rings [37]. This cluster can be regarded as an earth–moon system at the nanoscale. Cui *et al*. also further summarized the structural and electronic criteria for viable molecular rotors, highlighting fully delocalized π/σ electrons within boron rings or boron wheel motifs as a core prerequisite [35]. Very recently, Zhai's group theoretically designed a series of ternary nanoclusters rotors, including $MgTa_2B_6$, $CaBe_2B_7^-$, $Mg_2Be_2B_7^-$ clusters, whose rotational motion mimics miniature atomic clocks [–].

The successful examples mentioned above indicate that, in addition to strong electrostatic interactions, multiple π/σ aromaticity within the boron layer plays a vital role in multilayer molecular rotors. Whether boron layer exhibiting conflicting or antiaromatic character can also facilitate structural fluxionality remains an open question requiring systematic exploration. Inspired by the Ca_3B_8 molecular rotor reported by Guo's group [], herein we computational explore the potential energy surfaces (PESs) of the Ba_3B_8 cluster, which is a three-layered inverse-sandwich structure with conflicting aromaticity. The distorted heptacoordinate B_8 wheel is sandwiched by an upper Ba_2 dimer and an individual Ba atom at the bottom. Born-Oppenheimer molecular dynamics (BOMD) simulations reveal that the Ba_2 dimer can freely rotate with respect to the boron framework at the room temperature. Ba_3B_8 cluster can be formulated as $[Ba_2]^{2+}[B_8]^{4-}[Ba]^{2+}$ complex, due to the obviously charge transfer from the Ba_3 to B_8 motif. Bonding analysis reveals Ba_3B_8 cluster has 8π/6σ delocalized electrons, leading to a conflicting-aromatic system. This system establishes a prototypical molecular rotor stabilized by conflicting aromaticity and offers valuable guidelines for the rational design of molecular rotors in future studies.

2. Methods

Global-minimum structural searches were implemented *via* the unbiased Coalescence Kick (CK) algorithm [,], supplemented by manual structure construction. CK algorithm has been widely used for boron clusters and metal-doped boron clusters. In total, over 3,000 stationary points were probed at B3LYP/Lanl2dz level. The candidate low-lying isomers were then fully reoptimized at the B3LYP-D3/def2-TZVP level. Frequency calculations were also performed at the same level to confirm that the reported structures represent true minima on the potential energy surface, while transition states (TS) possess exactly one imaginary vibrational mode corresponding to the target rotational mode. To acquire accurate energetics for low-lying isomers and TS structure, single point CCSD(T)/def2-TZVP energy calculations were carried out on the top five most stable geometries []. Comparative calculations were also

conducted at the PBE0-D3/def2-TZVP level to check for consistency of different functionals in terms of structures and energetics. The def2-TZVP basis set was selected as a practical triple-zeta basis of broadly validated accuracy for molecular calculations involving both main-group and transition-metal elements.

The natural bond orbital (NBO) analysis was conducted at the B3LYP/def2-TZVP level to obtain the Wiberg bond indices (WBIs) and natural atomic charges, using the NBO 6.0 program []. Chemical bonding was illustrated using the canonical molecular orbital (CMO) analysis and adaptive natural density partitioning (AdNDP) []. AdNDP is an extended version of NBO analyses, which can describe the bonding in a molecule with n-center two-electron (nc-2e) bonds, which is suitable for description of the molecules featuring the multicenter bonds. Born-Oppenheimer molecular dynamics (BOMD) simulations were performed at PBE/DZVP-GHT level by means of the CP2K program []. The simulations were performed adiabatically, the initial velocity was not fixed but related to the temperatures considered, and the box size is 13 × 13 × 13 Å. The CMO and AdNDP data were visualized using the GaussView 5.0.9 and Molekel 5.4.0.8 programs [], respectively. Nucleus independent chemical shifts (NICSs) were calculated at the B3LYP/def2-TZVP level to assess the systems's π/σ aromaticity []. The magnetically induced ring current maps were generated using the anisotropy of current induced density (ACID) program [,]. Orbital compositions decomposition were completed using the Multiwfn 3.8 []. All the electronic structure calculations were accomplished using the Gaussian 09 package [].

3. Results

3.1. Global minimum structure and transition-state structures

Unbiased global PES searches combined with B3LYP-D3, PBE0-D3, and benchmark CCSD(T) calculations confirm that the C_s, (^{1}A') geometry represents the global minimum (GM) of Ba_3B_8 cluster. Alternative low-lying isomers are provided in Fig. S1 (**ESI†**). At all three theoretical levels, the C_s, (^{1}A') structure is consistently the GM structure. The nearest competitor turns out to be 1.24 kcal mol^{-1} higher in energy at CCSD(T) level. It is worth noting that the CCSD(T) method is the most reliable approach for boron-based nanoclusters. The third low-lying isomer featuring a B_8 ring exhibits markedly inferior thermodynamic stability. The other inverse-sandwich structure contains a B_8 ring rather than a B_8 wheel, and is 12.64 kcal mol^{-1} less stable than the GM. Therefore, the GM C_s (^{1}A') is confirmed to be the true minimum on the potential energy surface of the Ba_3B_8 cluster.

As illustrated in Fig. 1(a), the GM inverse-sandwich is composed of a distorted heptacoordinate B_8 wheel, being sandwiched by an upper Ba_2 dimer and an individual Ba atom at the bottom. The Ba_3 component is divided into the Ba_2 and Ba units. Overall, the GM Ba_3B_8 cluster has a diameter of 3.24 Å for B_8 wheel and a height of 5.16 Å, forming a subnanoscale inverse sandwich. Upon twisting the Ba_2

dimer relative to the B_8 wheel, a TS structure of Ba_3B_8 cluster is researched (Fig. 1(b)). The TS lies only 0.06 kcal mol^{-1} higher in energy than the GM at the B3LYP level, which is refined to 0.04 kcal mol^{-1} at the single-point CCSD(T). The negligible energy difference between the GM and TS hints the dynamic fluxional character of the Ba_3B_8 cluster.

3.2. Bond distances, Wiberg bond indices, and Natural atomic charges

To understand the thermodynamic stability of the GM Ba_3B_8 cluster, we reviewed the structural parameters as given in Fig. 2. Given the structural similarity between GM and TS geometries, the following analysis focuses primarily on the GM Ba_3B_8. Peripheral B–B bond distances along the B_8 wheel range from 1.54 to 1.57 Å (Fig. 2(a)). According to the recommended covalent radii, the upper limits of single B–B and double B=B are 1.70 and 1.56 Å, respectively []. For further reference, a typical B=B double bond is 1.51 Å []. The corresponding WBIs values for peripheral B–B bonds span 1.32 ~ 1.57 (Fig. 2(b)). Thus, the peripheral B–B bonds in GM Ba_3B_8 cluster are beyond single bond, indicating the presence of both Lewis-type σ bonds and delocalized π/σ bonds. The Ba–Ba distance within the Ba_2 dimer is 3.96 Å, which is close to the recommended distance of Ba–Ba single bond (3.92 Å). The calculated WBI is 0.90, confirming its authenticity as a single bond. The interlayer Ba–B distances span 2.86 ~ 3.24 Å with extremely small WBIs of 0.02 ~ 0.19, indicating the relatively weak covalent bonding between the Ba_2/Ba subunits and boron wheel. Such weak interlayer covalency is a critical structural prerequisite enabling the dynamic fluxional of the GM Ba_3B_8 cluster.

Natural atomic charges for GM Ba_3B_8 cluster are presented in Fig. 2(c). Boron possesses an electronegativity of 2.04, whereas barium exhibits a far lower value of merely 0.89. The substantial electronegativity difference between Ba and B governs the atomic charge distribution within the Ba_3B_8 cluster. The B atoms each carry a negative charge from −0.32 to −0.56 |e|. The B_8 wheel has a collective negative charge of −3.29 |e|, which can be approximately regarded as the B_8^{4-} charge state. The Ba_2 dimer carries a total positive charge of + 1.78 |e| and the bottom isolated Ba atom has + 1.53 |e|. The pronounced charge transfer from Ba_3 unit to the B_8 wheel rationalizes the ionic formulation $[Ba_2]^{2+}[B_8]^{4-}[Ba]^{2+}$. The bond distances, WBIs, and natural atomic charges for TS (Fig. S2, **ESI†**) are nearly identical to those of GM. Quantitatively, the B–B bond distances for GM and TS differ by less than ± 0.01 Å, and the corresponding B–B WBIs vary within ± 0.11. Meanwhile, both the Ba–Ba bond distance and WBI remains unchanged. Such negligible changes are in good agreement with a low rotational energy barrier.

4. Discussion

4.1. Dynamic Structural Fluxionality

According to vibrational frequency analysis, the GM Ba_3B_8 cluster has a soft vibrational mode of 14.9 cm^{-1} at B3LYP level (Fig. S3, **ESI†**). This soft mode corresponds to the rotation of the Ba_2 dimer relative to the B_8 wheel. To further confirm this mode, vibrational frequency calculations were also performed at the PBE0 level, identifying a soft mode at 22.2 cm^{-1}. Following this mode, a TS structure (C_s, $^1A'$) is reached with a soft imaginary vibrational mode, which is 20.7*i* and 29.2*i* cm^{-1} at the B3LYP and PBE0 levels, respectively.

The dynamic structural evolution of the GM Ba_3B_8 cluster is illustrated in Fig. 3, assuming that the Ba_2 dimer rotates counterclockwise around the distorted B_8 wheel. Starting from GM_1, the Ba_2 dimer undergoes a counterclockwise rotation of approximately 12.6° around the B_8 wheel, generating the first TS_1 structure. After traversing the energy barrier at TS_1, the Ba_2 dimer rotates another 12.6° to reach GM_2. The structural evolution pathway from GM_2 to GM_3 is identical to that observed from GM_1 to GM_2. Overall, the from GM_1 to GM_3, the Ba_2 dimer rotates by approximately one B–B bond (or 50.4°). Repeating this process seven times returns each atom to its initial position.

Born-Oppenheimer molecular dynamics (BOMD) simulations confirmed the above dynamic behavior [51]. The simulations were done at selected temperatures of 298, 500, and 600 K, at the PBE/DZVP level, starting from the equilibrium GM geometry with random velocities assigned to the atoms. During the simulations, the GM Ba_3B_8 cluster maintains sandwich structural integrity without fragment dissociation. As expected, the Ba_2 dimer floats above the B_8 wheel with unconstrained rotation. The simulation was done for 50ps. An extracted short movie from a simulation of over 30 ps at 298 K is present in the Supporting Information.

4.2. Chemical Bonding and Conflicting Aromaticity

To elucidate the thermodynamic stability and structural fluxionality of the GM Ba_3B_8 cluster, it is essential to conduct a detailed chemical bonding analysis. Canonical molecular orbitals (CMOs) of the GM are presented in Fig. 4, which are categorized into four subsets based on atomic orbital (AO) contributions. Among the 15 valence CMOs, only the HOMO in subset (d) originates primarily from Ba 6s AO, which has a major component of 89.4% from the Ba_2 dimer. It can be defined as a Ba–Ba σ bond. The remaining CMOs are primarily attributable to the distorted B_8 molecular wheel. Subset (c) includes 7 CMOs, composed of B 2s/2p AOs, which follow the orbital building principles with 0 up to 3 nodal planes. These CMOs represent seven two-center two-electron (2c-2e) peripheral B–B σ bonds on the B_8 wheel.

Subset (b) contains three delocalized σ orbitals on the B_8 wheel. Among them, HOMO−9 is completely delocalized and bonding, while the HOMO−4/HOMO−5 are partially bonding/anti-bonding orbitals. The 6σ electron counting satisfies the ($4n + 2$) Hückel rule, rendering σ aromaticity. Subset (a) shows four delocalized π orbitals. HOMO−2, HOMO−3, and HOMO−8 have minor orbital contribution from the Ba_3 unit (6.70%, 9.99%, and 9.86%). However, HOMO−1 has 36.3% contribution from the Ba_3 unit and 63.6%

from B_8 wheel, with the former showing strong 5d/6s hybridization. This unique orbital prevents the Ba_2 dimer from slipping off the B_8 wheel, which physically anchors the Ba_2 dimer atop the B_8 wheel, yet without hindering the rotor motion. The four delocalized π orbitals are intrinsically delocalized and cannot be transformed to Lewis-type bonds, which renders π antiaromaticity according to the ($4n$ + 2) Hückel rule. The 6σ-aromatic/8π-antiaromatic nature of the B_8 wheel gives rise to conflicting aromaticity, which is fully consistent with the formal $[B_8]^{4-}$ charge state.

AdNDP bonding analysis fully reproduces the above bonding picture [50]. As shown in Fig. 5 (a), the scheme completely recovers seven peripheral Lewis-type B–B σ bonds and one Ba–Ba σ bond in Ba_2 dimer. The occupation numbers (ONs) are greater than 1.90 |e|. The delocalized π/σ bonds are also reproduced. The σ sextet can be strictly partitioned as 8c-2e σ bonds in the B_8 wheel, whereas three out of the four delocalized π orbitals can be fully classified as 8c-2e π bonds. The remaining one π orbital is finally defined as an 11c-2e bond owing to the non-negligible contribution of the Ba_3 unit. Overall, GM Ba_3B_8 cluster is a conflicting aromatic system with 8π/6σ delocalized electrons. Its bonding characteristic is reminiscent of the B_8^{2-} cluster, which is a double aromaticity system with 6π/6σ electrons. Compared with the B_8^{2-} cluster, the B_8^{4-} motif possesses two additional π electrons, thereby rendering it 8π antiaromatic. The AdNDP scheme of TS structure for Ba_3B_8 cluster has been analyzed, which is similar to that of GM Ba_3B_8 (Fig. S4, **ESI†**).

NICS calculations [53] were carried out to independently evaluate the aromatic character (Table S2, **ESI†**). The large negative values of $NICS_{zz}(0)$ and $NICS_{zz}(1)$ represent σ and π aromaticity, respectively. $NICS_{zz}(0)$ at the B_3 triangle center are strongly negative values, confirming that the GM Ba_3B_8 cluster is indeed σ aromaticity. The $NICS_{zz}(1)$ value is computed at 1 Å above the center of B_3 triangle. Notably, a distinctly positive value is observed for only one of the boron triangles, which suggests a certain degree of antiaromatic character. The sign changes of $NICS_{zz}(1)$ values for the other B_3 triangular can be attributed to the effect of the heavy atom Ba. It should be emphasized, however, that the antiaromaticity of the Ba_3B_8 cluster is primarily established on the basis of the four delocalized π orbitals, which represent the fundamental criterion for aromaticity evaluation in boron-based nanoclusters.

To confirm the antiaromatic characteristic of the Ba_3B_8 cluster, the ring current calculations were performed using the AICD (anisotropy of the induced current density) program [54,55]. The AICD calculations were decomposed into σ and π contributions by selecting occupied σ-type and π-type molecular orbitals separately. Figure 6 displays the total ring current of the system (Fig. 6 (a)) as well as the σ and π electrons contributions to the ring current (Fig. 6(b) and 6(c)). It can be observed that σ electrons induce diatropic currents, which verifies the σ aromatic character of the Ba_3B_8 cluster. In contrast, the π current density map (Fig. 6(c)) exhibits a counterclockwise ring current, revealing π antiaromaticity of this system. These current density maps further confirm the conflicting aromatic nature of the Ba_3B_8 cluster.

We briefly discuss some aspects of the Ba_3B_8 molecular rotor. First, the Ba_3 component is not stacked into a triangle but is divided into Ba_2 dimer and an isolated Ba atom. Such a distribution pattern promotes interlayer charge transfer. Second, in the previously reported three-layer sandwich-type rotor, strong charge transfer originating from metal to boron motifs, endowing the boron ring or boron wheel with double π/σ aromaticity (such as $Na_6B_7^-$, $Na_8B_7^+$). Nevertheless, the present Ba_3B_8 cluster represents a unique molecular rotor with $[Ba_2]^{2+}[B_8]^{4-}[Ba]^{2+}$ ionic configurations, which induces 8π/6σ conflicting aromatic behaviors in the middle B_8 wheel. This system demonstrates that conflicting-aromatic boron motifs can also support fluxional behavior, provided that strong interlayer electrostatic stabilization maintains the structural integrity of the three-layer framework. Third, it is generally considered that weakly bound clusters tend to display fluxional behavior. However, the GM Ba_3B_8 cluster cannot be categorized as a weakly bound cluster. Lastly, the Ba_2 dimer does not slip away from B_8 disk. This is ascribed to the HOMO−1 orbital in Fig. 4. The π bond involves a contribution of 18.5% from center B atom, which effectively anchors the Ba_2 dimer on the B_8 disk.

4.3. Interaction energies

To quantify the interlayer binding strength between the Ba_2/Ba and the central B_8 wheel in GM Ba_3B_8 cluster, we artificially displaced Ba_2/Ba and B_8 wheel to a separation of 10 Å and single-point energies were calculated at B3LYP/def2-TZVP. The energy difference, with respect to the GM structure, reaches 15.8 eV, demonstrating exceptionally strong electrostatic interactions. We stress that the above estimate is qualitative rather than quantitative. This massive electrostatic binding stabilizes the three-layer architecture, while the weak covalent Ba–B bonds are non-negligible for the dynamic fluxionality of the Ba_3B_8 cluster. Whereas most boron-based nanorotors reported to date rely on double aromaticity to stabilize the middle boron layer, the Ba_3B_8 system unambiguously illustrates that conflicting aromaticity (8π/6σ) can also sustain dynamics fluxionality, on the premise that the middle boron layer retains structural rigidity and hosts strong interlayer electrostatic interactions.

5. Conclusions

In conclusion, we have theoretically investigated a unique three-layer inverse sandwich molecular rotor, Ba_3B_8, composed of a distorted B_8 wheel, a Ba_2 dimer at the top, and an isolated Ba atom at the bottom. Natural atomic charge analysis reveals that the system can be described as $[Ba_2]^{2+}[B_8]^{4-}[Ba]^{2+}$ ionic complex, wherein the central B_8 wheel exhibits 8π/6σ conflicting aromaticity. This unique bonding pattern endows the system with remarkable structural fluxionality, facilitating nearly free rotation of the Ba_2 dimer around the distorted B_8 wheel at room temperature. In contrast to previously reported boron-based molecular rotors stabilized by double aromaticity, the Ba_3B_8 cluster represents an exceptional case featuring conflicting aromaticity. This work enriches the family of boron nanoclusters and provides new strategies for designing molecular machines with distinctive electronic structures.

Declarations

Author Contribution

Shuting Zhang, Lizhao Fan, and Xiaobo Hu calculated low-lying isomers.Yuzhen Du, Tinglu Zhang, and Yingchao Ma analyzed the chemical bonding of the Ba3B8 cluster.Jinglu Guo and Jingying Li prepared figures 1-6Changqing Miao and Yingjin Wang revised the manuscript. Linyan Feng wrote the main manuscript text.All authors reviewed the manuscript

Acknowledgements

This work was supported by the Natural Science Foundation of Shanxi Province (No. 202303021212298, 202203021222305), the Natural Science Foundation of Xinzhou (No. 20240508), the College Student Innovation Training Program in Shanxi Province (20251313), and the Xinzhou Normal University (2021KY04).

References

1. Aihara J, Kanno H, Ishida T (2005) Aromaticity of planar boron clusters confirmed. J Am Chem Soc 127:13324–13330. https://doi.org/10.1021/ja053171i
2. Jian T, Chen XN, Li SD, Boldyrev AI, Li J, Wang LS (2019) Probing the structures and bonding of size-selected boron and doped-boron clusters. Chem Soc Rev 48:3350–3591. https://doi.org/10.1039/c9cs00233b
3. Jiménez-Halla JOC, Islas R, Heine T, Merino G (2010) B_{19}^-: an aromatic wankel motor. Angew Chem Int Ed, 49:5668 – 5671. https://doi.org/10.1002/anie.201001275
4. Martínez-Guajardo G, Sergeeva AP, Boldyrev AI, Heine T, Ugalde JM, Merino G (2011) Unravelling phenomenon of internal rotation in B_{13}^+ through chemical bonding analysis. Chem Commun 47:6242 – 6244. https://doi.org/10.1039/c1cc10821b
5. Moreno D, Pan S, Zeonjuk LL, Islas R, Osorio E, Martínez-Guajardo G, Chattaraj PK, Heine T, Merino G (2014) B_{18}^{2-}: a quasi-planar bowl member of the Wankel motor family. Chem Commun 50:8140 – 8143. https://doi.org/10.1039/c4cc02225d
6. Fagiani M, Song XW, Petkov P, Debnath S, Gewinner S, Schollkopf W, Heine T, Fielicke A, Asmis KR (2017) Structure and fluxionality of B_{13}^+ probed by infrared photodissociation spectroscopy. Angew Chem Int Ed 56:501 – 504. https://doi.org/10.1002/anie.201609766
7. Wang Y, Zhao XY, Chen Q, Zhai HJ, Li SD (2015) B_{11}^-: a moving subnanoscale tank tread. Nanoscale 7:16054 – 16060. https://doi.org/10.1039/c5nr03732h
8. Wang YJ, You XR, Chen Q, Feng LY, Wang K, Ou T, Zhao XY, Zhai HJ, Li SD (2016) Chemical bonding and dynamic fluxionality of a B_{15}^+ cluster: a nanoscale double-axle tank tread. Phys Chem Chem

Phys 18:15774 – 15782. https://doi.org/10.1039/c6cp02544g

9. Ito K, Pu Z, Li QS, Schleyer PvR (2008) Cyclic boron clusters enclosing planar hypercoordinate cobalt, iron, and nickel. Inorg Chem 47:10906 – 10910. https://doi.org/10.1021/ic800993b
10. Liu FL, Gao SJ. Zhai HJ (2025) Boron-based $B_3Zn_6^-$ alloy cluster as a hybrid between prismatic and sandwich-like structures: stabilization of a linear B_3 chain motif using electronic transmutation. J Chem Phys 162:114304. https://doi.org/10.1063/5.0257359
11. Wang YJ, Feng LY, Guo JC, Zhai HJ (2017) Dynamic Mg_2B_8 cluster: a nanoscale compass. Chem Asian J 12:2899–2903. https://doi.org/10.1002/asia.201701310
12. Zhang XY, Guo JC (2020) Dynamic fluxionality of ternary Mg_2BeB_8 cluster: a nanocompass. J Mol Model 26:30. https://doi.org/10.1007/s00894-020-4292-0
13. Guo JC, Feng LY, Wang YJ, Jalife S, Vásquez-Espinal A, Cabellos JL, Pan S, Merino G, Zhai HJ (2017) Coaxial triple-layered versus helical $Be_6B_{11}^-$ clusters: dual structural fluxionality and multifold aromaticity. Angew Chem Int Ed 56:10174–10177. https://doi.org/10.1002/anie.201703979
14. Wang YJ, Feng LY, Xu L, Hou XR, Li N, Miao CQ, Zhai HJ (2020) Boron-based ternary $Rb_6Be_2B_6$ cluster featuring unique sandwich geometry and a naked hexagonal boron ring. Phys Chem Chem Phys 22:20043–20049. https://doi.org/10.1039/d0cp03123b
15. Liu FL, Guo JC, Zhai HJ (2024) Boron-based ternary $MgTa_2B_6$ cluster: a turning nanoclock with dynamic structural fluxionality. Phys Chem Chem Phys 26:6049–6057. https://doi.org/10.1039/d3cp05826c
16. Liu FL, Bai LX, Guo JC, Zhai HJ (2025) Ternary $CaBe_2B_7^-$ cluster: a turning nanoclock. J Phys Chem A 129:4667–4672. https://doi.org/10.1021/acs.jpca.5c01601
17. Li YX, Cheng YX, Guo JC (2025) Theoretical study of the conflicting-aromatic Ca_3B_8 nanocluster rotor. Chem J Chinese Universities 46:20250149. https://doi.org/10.7503/cjcu20250149
18. Tai TB, Nguyen MT, Dixon DA (2010) Thermochemical properties and electronic structure of boron oxides B_nO_m (n = 5–10, m = 1–2) and their anions. J Phys Chem A 114:2893–2912. https://doi.org/10.1021/jp909512m
19. Saunders M (2004) Stochastic search for isomers on a quantum mechanical surface. J Comput Chem 25:621–626. https://doi.org/10.1002/jcc.10407
20. Bartlett RJ, Musial M (2007) Coupled-cluster theory in quantum chemistry, Rev Mod Phys 79:291–352. https://doi.org/10.1103/RevModPhys.79.291
21. Glendening ED, Badenhoop JK, Reed AE, Carpenter JE, Bohmann JA, Morales CM, Landis CR, Weinhold F (2013) NBO 6.0, Theoretical Chemistry Institute, University of Wisconsin, Madison.
22. Zubarev DY, Boldyrev AI (2008) Developing paradigms of chemical bonding: adaptive natural density partitioning. Phys Chem Chem Phys 10:5207–5217. https://doi.org/10.1039/b804083d
23. Kuhne TD, Lanuzzi M, Ben MD, Rybkin VV, Seewald P, Stein F, Laino T, Khaliullin RZ, Schütt O, Schiffmann F, Golze D, Wilhelm J, Chulkov S, Bani-Hashemian MH, Weber V, Borštnik U, Taillefumier

M, Jakobovits AS, Lazzaro A, Pabst H, Müller T, Schade R, Guidon M, Andermatt S, Holmberg N, Schenter GK, Hehn A, Bussy A, Belleflamme F, Tabacchi G, Glöß A, Lass M, Bethune I, Mundy CJ, Plessl C, Watkins M, VandeVondele J, Krack M, Hutter J (2020) CP2K: an electronic structure and molecular dynamics software package-Quickstep: efficient and accurate electronic structure calculations. J Chem Phys 152:194103. https://doi.org/10.1063/5.0007045

24. Varetto U (2009) Molekel 5.4.0.8, Swiss National Supercomputing Center, Manno, Switzerland.
25. Chen Z, Wannere CS, Corminboeuf C, Puchta R, Schleyer PvR (2005) Nucleus-independent chemical shifts (NICS) as an aromaticity criterion. Chem Rev 105:3842–3888. https://doi.org/10.1021/cr030088+
26. Herges R, Geuenich D (2001) Delocalization of electrons in molecules. J Phys Chem A 105:3214–3220. https://doi.org/10.1021/jp0034426
27. Geuenich D, Hess K, Köhler F, Herges R (2005) Anisotropy of the induced current density (ACID), a general method to quantify and visualize electronic delocalization. Chem Rev 105:3758–3772. https://doi.org/10.1021/cr0300901
28. Lu T, Chen F (2012) Multiwfn: a multifunctional wavefunction analyzer, J Comput Chem 33:580–592. https://doi.org/10.1002/jcc.22885
29. Frisch MJ, Trucks GW, Schlegel HB, et al. (2009) Gaussian 09, revision D.01; Gaussian, Inc.: Wallingford, CT.
30. Pyykkö P. (2015) Additive covalent radii for single-, double-, and triple-bonded molecules and tetrahedrally bonded crystals: a summary. J Phys Chem A 119:2326–2337. https://doi.org/10.1021/jp5065819
31. Li SD, Zhai HJ, Wang LS (2008) $B_2(BO)_2^{2-}$ — diboronyl diborene: a linear molecule with a triple boron-boron bond. J. Am. Chem. Soc. 130:2573–2579. https://doi.org/10.1021/ja0771080

Figures

Figure 1.

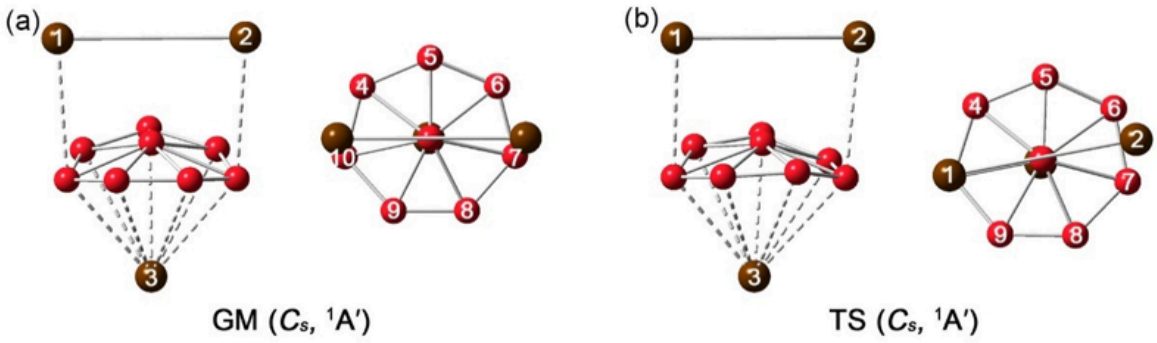


Figure 1

Optimized structures of (a) C_s (^{1}A¢) global minimum (GM) and (b) C_s (^{1}A¢) transition state (TS) of the Ba_3B_8 cluster at the B3LYP/def2-TZVP level. Both top- and side-views are presented. The B atoms are illustrated in red color and Ba in brown.

Figure 2.

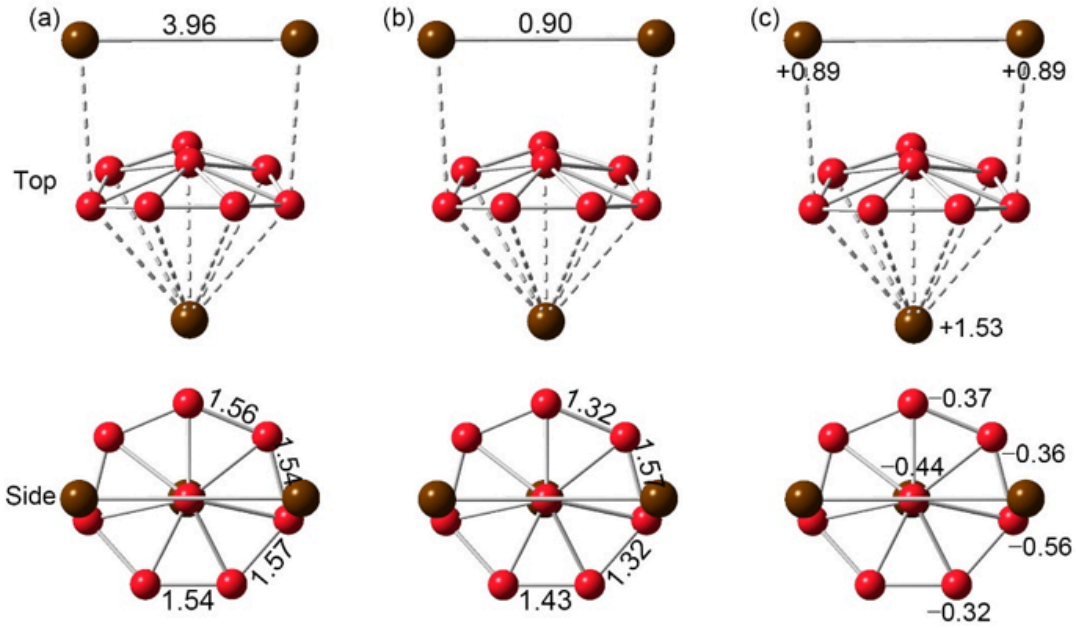


Figure 2

Calculated (a) bond distances (in Å), (b) Wiberg bond indices (WBIs), and (c) natural atomic charges (in |e|) for GM Ba_3B_8 cluster at B3LYP/def2-TZVP level.

Figure 3.

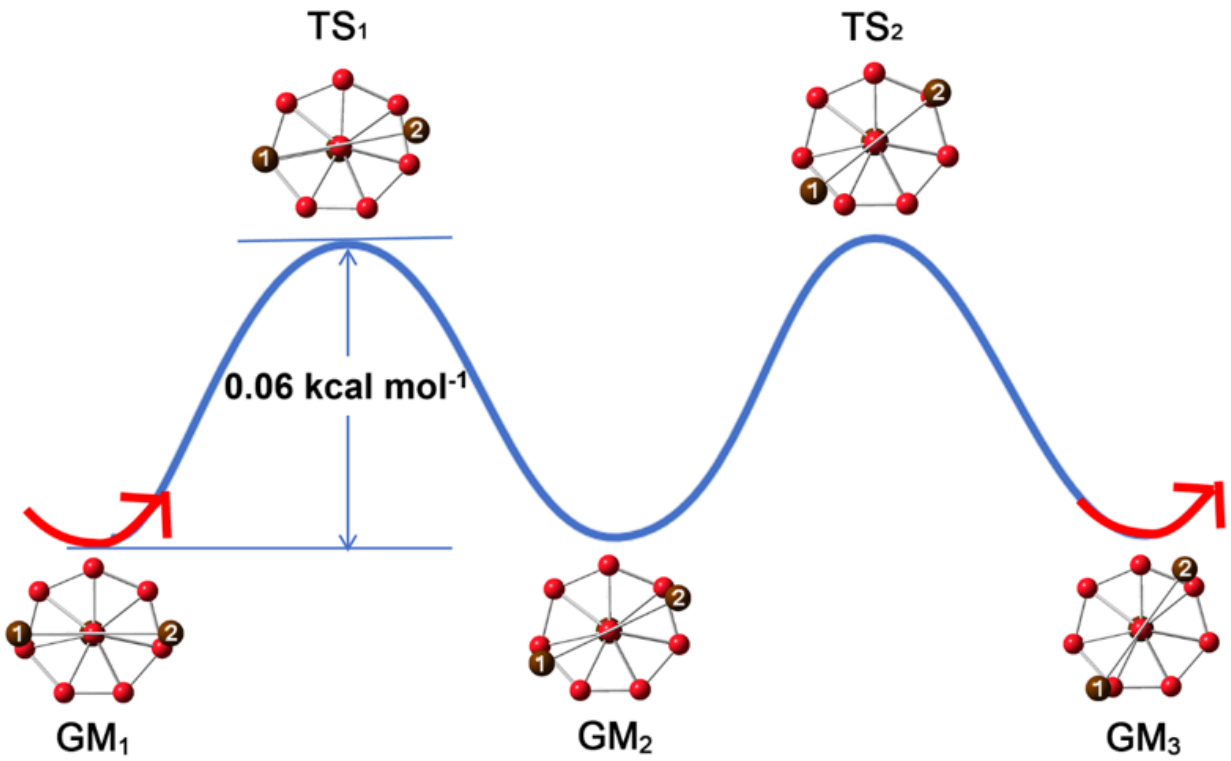


Figure 3

Structural evolution of Ba_3B_8 cluster during the dynamic rotation of Ba_2 dimer with respect to the B_8 baseplate. The Ba_2 dimer is assumed to rotate anticlockwise in the presentation.

Figure 4.

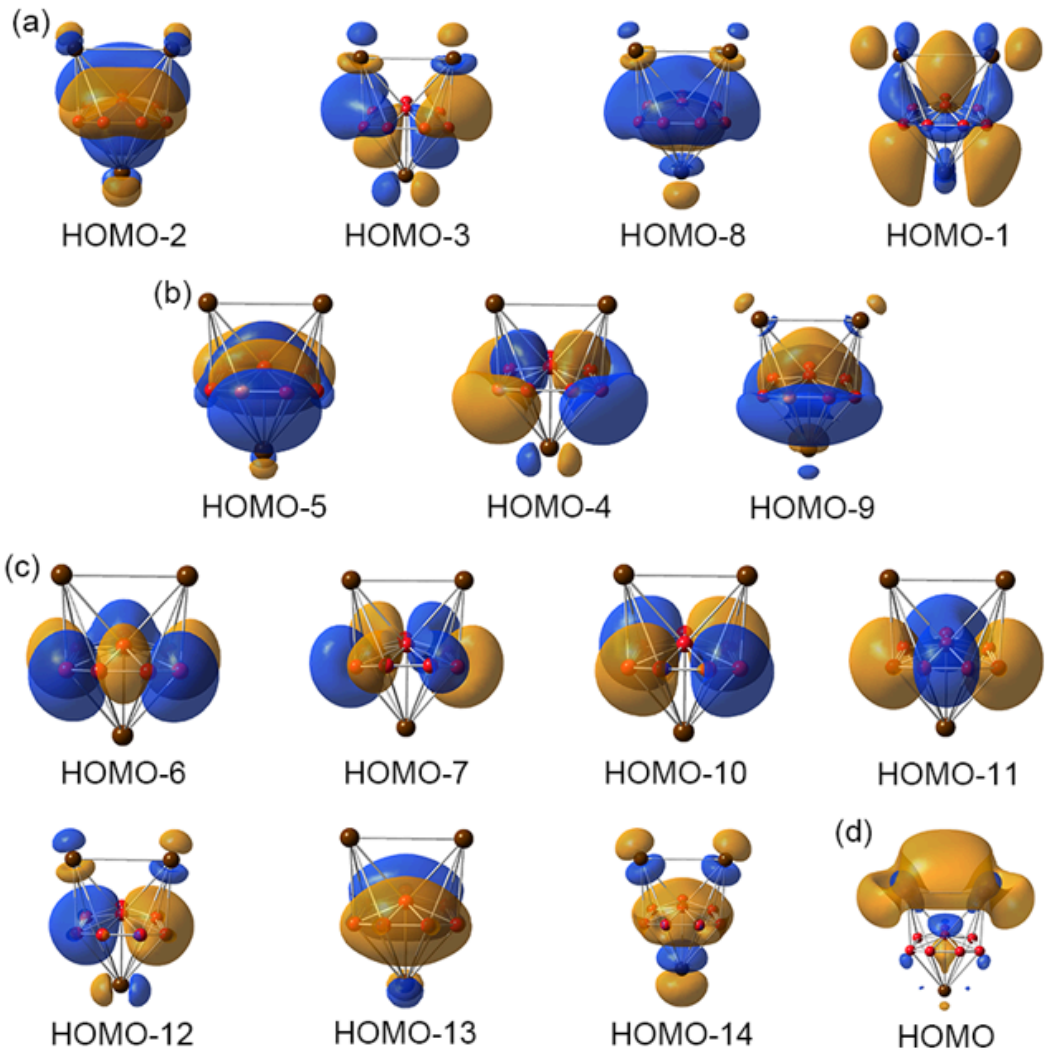


Figure 4

Canonical molecular orbitals (CMOs) of the C_s (^{1}A¢) GM structure of Ba_3B_8 cluster. (a) Four delocalized π CMOs. (b) Three delocalized σ CMOs. (c) Seven CMOs for localized B-B σ bonds in the periphery of B_8 wheel. (d) One σ bond within the Ba_2 dimer.

Figure 5.

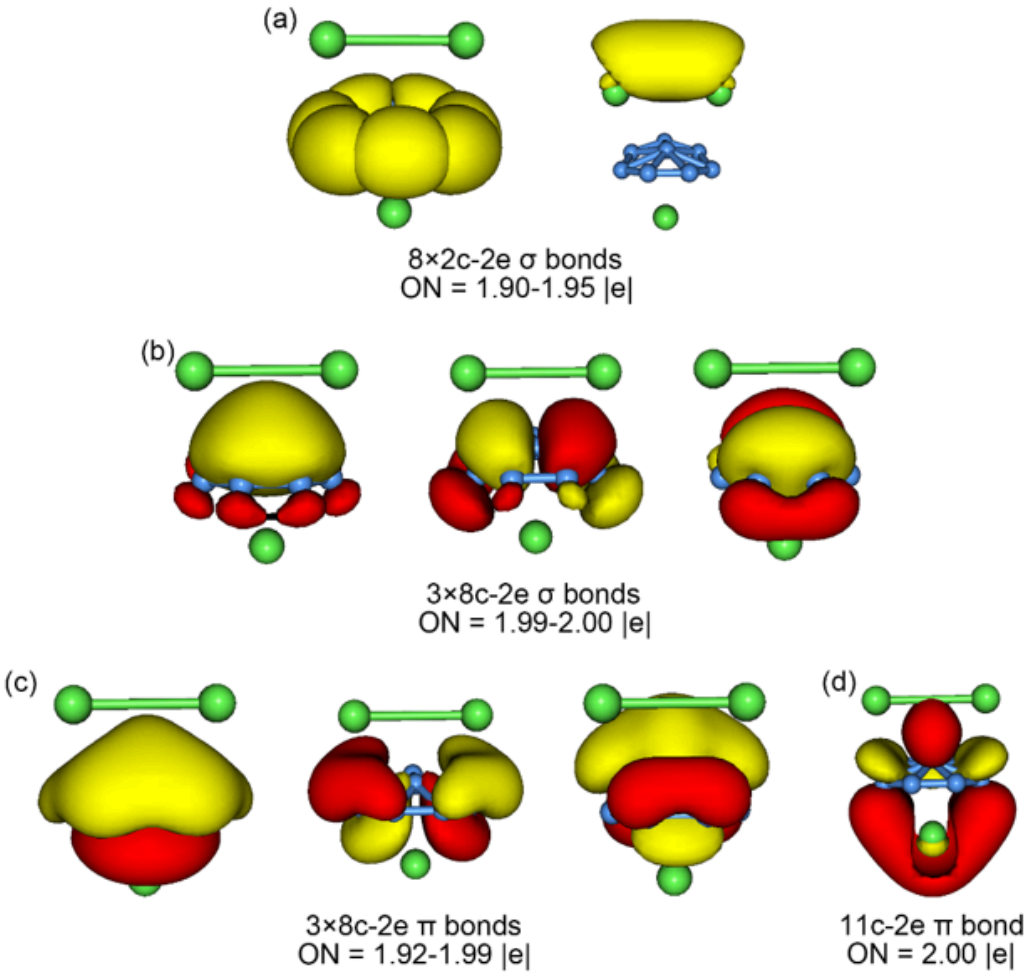


Figure 5

Chemical bonding pattern of GM (C_s, ^{1}A¢) on the basis of adaptive natural density partitioning (AdNDP) analysis. ONs are indicated.

Figure 6.

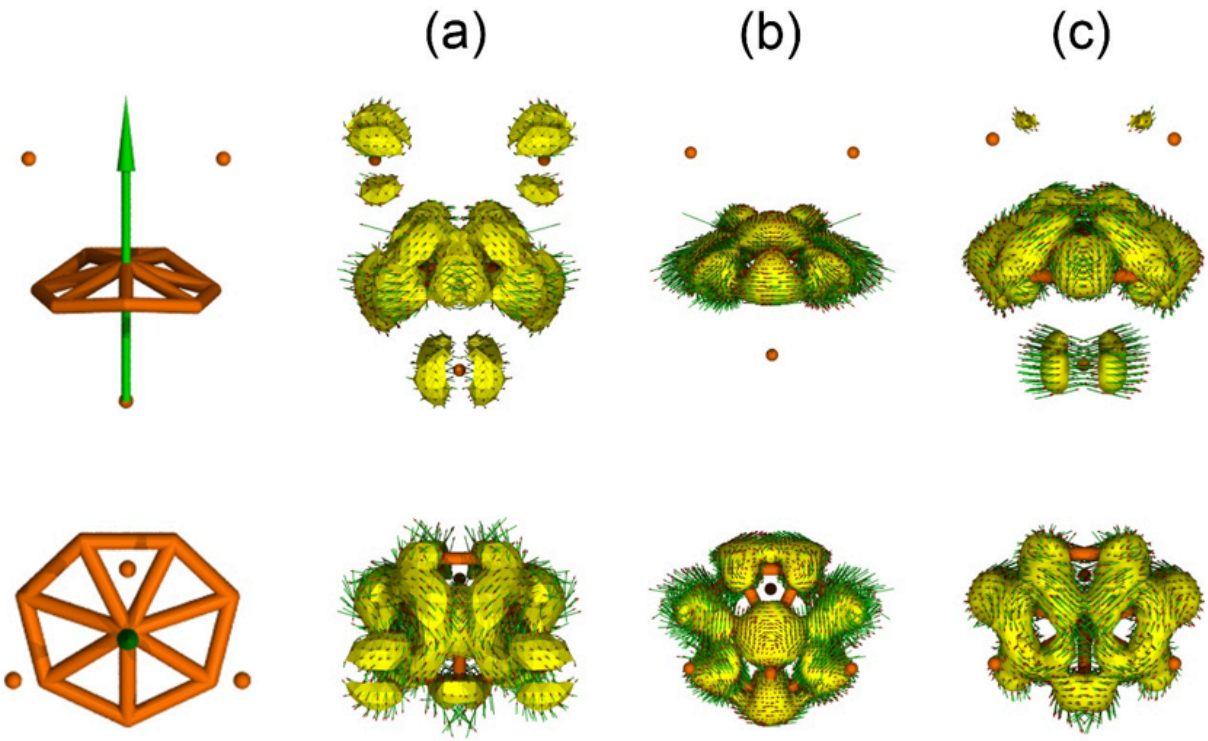


Figure 6

Total ring current (a), σ ring current (b), and π ring current maps for Ba_3B_8 cluster calculated at an isosurface value of 0.05. Both top and side-view representations are shown.

Supplementary Files

This is a list of supplementary files associated with this preprint. Click to download.

- Ba3B8ESIJMolModelfinal.docx
- B8Ba3bomd298KJMolModelfinal.mp4